RSC Advances

PAPER

View Article Online
View Journal | View Issue

Cite this: *RSC Adv.*, 2022, **12**, 10267

MXene-regulation polyamide membrane featuring with bubble-like nodule for efficient dye/salt separation and antifouling performance†

Yuanyuan Wang,[a] Hang Xu, *[a] Mingmei Ding,[a] Lei Zhang,[b] Gang Chen,[c] Jiawei Fu,[a] Ao Wang,[a] Jiapei Chen,[a] Bonan Liu[a] and Wen Yang[a]

Received 17th January 2022
Accepted 25th March 2022

DOI: 10.1039/d2ra00335j

rsc.li/rsc-advances

Removing salt from dye/salt mixtures using nanofiltration (NF) membranes needs to be improved to ensure high permeability, high selectivity, and antifouling performance. In this study, we used an interfacial polymerization (IP) technique to create a novel thin-film nanocomposite NF membrane by introducing two-dimensional MXene $Ti_3C_2T_x$ into the polyamide (PA) layer. Enhanced IP reaction rate facilitated the overflow of residual solvent from the fresh PA layer's edge due to the MXene-mediated IP strategy, resulting considerable bubble-like nodules on the membrane surface. The unique nanostructure of PA effective layer could be tuned by controlling the MXene concentration in aqueous phase solution, which finally promoted the obtained membranes with superb permselectivity. In this way, the water permeability was elevated to a maximum value of 45.12 L m^{-1} h^{-1}, nearly 1.58-fold compared to the PA-pristine membrane. Moreover, the $Ti_3C_2T_x$/NF membrane exhibited a superior dye/monovalent salt separation coefficient of 820, outperforming the pristine PA membrane and other NF membranes in the literature. Additionally, the MXene-assisted IP strategy designed an effective dye anti-fouling hydration layer, which played a crucial role in fouling resistance. This work illustrates a novel use of $Ti_3C_2T_x$ to successfully regulate high-performance TFN PA membranes for potential application in dye/salt separation.

1. Introduction

In the traditional chemical production of dyes, salt (sodium chloride; NaCl) and other small molecular weight intermediates were utilized as reaction promoters; and electrolyte (salt) was further employed for the precipitation of dyes from aqueous solutions, known as the salting-out process. However, the final dye product obtained from the conventional process is of low purity due to the presence of NaCl (nearly 30%), which could not meet the needs of highly purification.[1–3] In addition, the traditional manufacturing process is labor-intensive, with high energy consumption and severe environmental pollution.[4,5] Therefore, it is imperative to develop an efficient platform for the purification of dyes. Nanofiltration (NF) as a pressure-driven membrane filtration process has gained extensive attention in the file of purification due to its advantages of low energy consumption and environmental friendliness. It is generally recognized that the interception capacity of NF membrane is established by a combination of the Donnan effect and the sieving effect, wherein the retention rate is higher for salts with multivalent anionic and organics with molecular weight more than 300, while lower for salts with monovalent anions and non-ionized organics with molecular weights less than 150.[4,6–8] Therefore, NF would be an up-and-coming technology for the replacement of the traditional salting-out process by simultaneously removing NaCl and increasing the concentration of aqueous dye solutions.[9] However, membrane fouling was a stumbling block to NF, which reduced permeability of the required molecules, decreased rejection performance, and ultimately shortened the service life of membranes.[10–13] It is an urgent demand to fabricate NF membranes with superior anti-fouling ability for effectively fractionation of dyes and NaCl.

Commercial NF membranes are thin-film composite (TFC) membranes with polyamide (PA) as the functional layer. The ultrathin selective layer allows TFC membranes to have a higher dye/monovalent salt ion separation efficiency. However, the trade-off effect between water permeability and salt rejection is still a challenge for the wide application of TFC membranes.[14] Previous research has revealed that the PA layer's properties are critical for TFC-NF membrane's permeability and selectivity.[12,15] With the rapid development of nanotechnology, 2D nanomaterials such as graphene oxide,[16] molybdenum disulfide,[17] carbon nitride[18] and boron nitride nanosheets,[19] were gradually

---

[a] *Key Laboratory of Integrated Regulation and Resource Development on Shallow Lakes, Ministry of Education, College of Environment, Hohai University, Nanjing 210098, China. E-mail: xuhang810826@163.com*

[b] *College of Civil and Architecture Engineering, Chuzhou University, Chuzhou 239000, China*

[c] *State Key Laboratory of Hydrology-Water Resources and Hydraulic Engineering, College of Hydrology and Water Resources, Hohai University, Nanjing 210098, China*

† Electronic supplementary information (ESI) available. See DOI: 10.1039/d2ra00335j

applied for the regulation of PA layer due to their atomic-level thickness, mechanical properties, multifunctional groups, and to provide high-speed water channels. After incorporating with 2D nanomaterials, the physicochemical properties of PA layer including surface roughness, hydrophilic properties, surface charge, and cross-link density could be elaborately regulated, facilitating the separation performance.[20] Moreover, the vulnerability of PA membranes to fouling is mainly related to the hydrophobicity of the PA active layer. The incorporation of nanomaterials tends to facilitate the formation of a stable and continuous hydration layer, which is of great significance for increasing anti-fouling property of PA layer.[21,22]

MXene (transition metal carbonitride), as a new type of 2D nanomaterial with good hydrophilicity, tunable electronegativity, and mechanical properties, exhibited great potential for desalination and dye separation.[23–26] The unique structure of MXene nanosheets ensures sufficient strength during the separation process. The low concentration and good dispersion of MXene supernatant exhibit good affinity and interface compatibility with the PA matrix. In addition, the negatively charged hydrophilic groups on the surface of MXene can facilitate the rejection ability of anions and the resistance to contamination.[27–29] Wang *et al.*[30] doped MXene nanosheets into a PA layer *via* interfacial polymerization (IP), and the resulting reverse osmosis (RO) membrane showed excellent water flux and chlorine resistance. Xue *et al.*[31] used MXene supernatant containing several layers as an aqueous phase solvent for interfacial polymerization. The prepared MXene composite NF membranes exhibited excellent low-carbon and persistent desalination performance. However, the regulation mechanism of MXene embedding on PA layer has not been well investigated. Besides, little optimization work has been conducted on introducing MXene into the PA layer for dye/salt separation, and further research is required.

In this study, we proposed a facile MXene-assisted IP strategy of designing TFN membranes for enhanced dye/salt separation and antifouling performance. The presence of MXene nanosheets significantly increased the PIP adsorption with enhanced IP reaction rate, and residual solvent flows spilled out from the edges of fresh PA layer, resulting in the formation of bubble-like nodules on the membrane surface. This special nano-structure endowed the PA effective layer with an increased effective permeable area, while the introduction of MXene nanosheets reduced the formation of non-selective pores, therefore the corresponding nodule-type NF membrane exhibited higher water permeability and ultrahigh dye/monovalent salt selectivity. Besides, the introduction of MXene facilitated the combination with water molecules through hydrogen bond; a novel dye anti-fouling hydration layer was constructed on the membrane surface, thereby promoting higher surface hydrophilicity and anti-fouling properties. MXene nanocomposite membranes will pave the way for dye/salt separation NF membranes in the future.

2. Experimental

2.1 Materials and chemicals

Piperazine (PIP; 99%) and lithium fluoride (LiF; 99%) were purchased from Rhawn Co., Ltd (Shanghai, China). Trimesoyl chloride (TMC; 98%), sodium sulfate (Na_2SO_4), and NaCl were acquired from Aladdin Co., Ltd (Shanghai, China). *N*-Hexane (97%) and polyethylene glycol (PEG; 200, 400, 600, and 800 Da) were provided from Shanghai Macklin Biochemical Co., Ltd (Shanghai, China). Magnesium sulfate ($MgSO_4$) was purchased from Shanghai HUSHI Co., Ltd (Shanghai, China). Congo red (CR) was provided by YUANYE Bio-Technology Co., Ltd (Shanghai, China). Methylene blue (MB) was acquired from MAIKUN Chemical Co., Ltd (Shanghai, China). All of these chemicals were used without further purification.

Titanium aluminum carbide powder (Ti_3AlC_2, 99%, 300 mesh) was acquired from Nanjing Mission New Materials Co., Ltd (Nanjing, China). A polysulfone (PSF) ultrafiltration membrane (DelStar Technologies Co., Ltd, Suzhou, China) was used as support. Throughout the experiments, deionized water was used.

2.2 Fabrication of $Ti_3C_2T_x$ and preparation of membranes

2.2.1 Fabrication of $Ti_3C_2T_x$. First, LiF (1 g) was added to hydrogen chloride solution (15 mL, 9 mol L^{-1}), which was then stirred for 10 min at 25 °C. The mixture was then gradually supplemented with one gram of Ti_3AlC_2 powder, which was kept at 35 °C for 24 h. Subsequently, the mixture was centrifuged and rinsed with deionized water to reach a neutral pH. The $Ti_3C_2T_x$ slurry was collected and re-dispersed in 100 mL of deionized water. For delamination, the mixture was sonicated in flowing nitrogen for 1 h. Finally, a stable MXene colloidal solution (7.9 g L^{-1}) was obtained by centrifuging the suspension at 3500 rpm for 30 min.

2.2.2 Preparation of $Ti_3C_2T_x$/NF membranes. Interfacial polymerized PA membranes were prepared on PSF membranes. To eliminate sodium nitrite contamination, the PSF membranes were submerged in deionized water for 24 h. After that, the membranes were attached to a plate framework, and the PIP solution was placed to the support for 5 min. The excess PIP solution was then removed with a rubber roller. Subsequently, the TMC solution was poured onto the support. The resultant nanocomposite membranes were rinsed with deionized water after 2 min to eliminate any remaining chemicals. Finally, the produced membranes were heated for 3 min at 60 °C before being kept in deionized water for further research. The optimized monomer concentrations were 0.750 wt% and 0.038 wt% for PIP and TMC, respectively. $Ti_3C_2T_x$ was uniformly dispersed into the PIP solution at 0.001, 0.002, 0.005, and 0.010 wt% after ultrasonication for 30 min, which were denoted as M0, M1, M2, M3, and M4, respectively.

2.3 Microstructural characterization

The structures of Ti_3AlC_2 and $Ti_3C_2T_x$ were characterized using scanning electron microscopy (SEM; Hitachi S4800, Japan) and transmission electron microscopy (TEM; JEOL JEM-2100F, Japan). The monolayer structure of $Ti_3C_2T_x$ was determined using atomic force microscopy (AFM; Bruker Icon, Germany). To identify the crystal structure and d-spacing of the product, the raw materials and products were analyzed using X-ray diffraction (XRD; Bruker D8 Advance, Germany).

The morphology of the $Ti_3C_2T_x$/NF membranes was observed using SEM (Hitachi S4800, Japan). Elemental distribution of samples was determined using an EDS (Octane Plus, USA) equipped on SEM. The roughness of the membranes was measured by AFM (Bruker Icon, Germany). The chemical compositions of the produced membranes were determined using X-ray photoelectron spectroscopy (XPS; Thermo ESCALAB 250Xi, USA), and their functional chemical structures were investigated using attenuated total reflectance-Fourier transform infrared spectroscopy (FTIR; PerkinElmer Spectrum 100, USA). To analyze the surface wetting nature of the membranes, contact angle goniometry (Dataphysics OCA15EC, Germany) was utilized to monitor water contact angle. The zeta potential of the $Ti_3C_2T_x$/NF membranes was determined using a laser particle size analyzer (Malvern Mastersizer 3000, UK).

2.4 NF performance test

The dead-end membrane test unit was utilized for the permeability and rejection tests (HP 4750 high-pressure stirred cell, Sterlitech). Compared with the complex cross-flow system, dead-end stirred cells were more convenient, achieving a similar permeate flux with the same membrane sheet.[32] The membrane sample was compressed for 30 min before the test to reach steady state. The water flux was then determined by the volume of water filtered over time at 0.35 MPa (3.5 bar). Salt solutions with a concentration of 2000 ppm were used to investigate salt rejection. The following formulas were used to determine the water flux (F) and salt rejection (R):

$$F = \frac{V}{A \times t} \tag{1}$$

$$R = \left(1 - \frac{C_p}{C_f}\right) \times 100\% \tag{2}$$

where F is the permeate flux (L m^{-2} h^{-1}), V is the permeate volume (L), A is the effective separation area (m^2), and t is the permeation time (h). C_p and C_f represent the salt concentrations in the permeate and the feed, respectively. To determine the salt concentration, the conductivity of the salt solution was measured with a conductivity meter.

2.5 Molecular weight cutoff and dye rejection test

The molecular weight cutoff (MWCO) of the PA and $Ti_3C_2T_x$/NF membranes was measured using 1000 ppm PEG solutions with different molecular weights (200, 400, 600, and 800 Da). PEG concentrations in the feed and permeate were measured using a TOC analyzer (O. I. Analytical Aurora Model 1030, USA). The MWCO was calculated according to the molecular weight, where the rejection was approximately 90%. The Stokes radius of PEG was calculated using the following equation:

$$r_s = 16.73 \times 10^{-3} \times M^{0.557} \tag{3}$$

where M is the molecular weight of the PEG solute and r_s (nm) is the Stokes radius.

The rejection mechanism of NF membranes is also impacted by electrostatic interactions; thus, four different dyes (Methyl Orange, MO; Methylene Blue, MB; Congo Red, CR; and Crystal Violet, CV) were tested at neutral pH in the experiment. The dye rejection (R) was calculated as eqn (2). A dye rejection test using NaCl/Congo Red (CR) and NaCl/Crystal Violet (CV) mixture solutions was performed to examine the NaCl/dye selectivity of the prepared membranes. The NaCl and dye concentrations were 2000 ppm and 100 ppm, respectively. The following equation was used to calculate the selectivity of NaCl for dyes:

$$\alpha = \frac{1 - R_A}{1 - R_B} \tag{4}$$

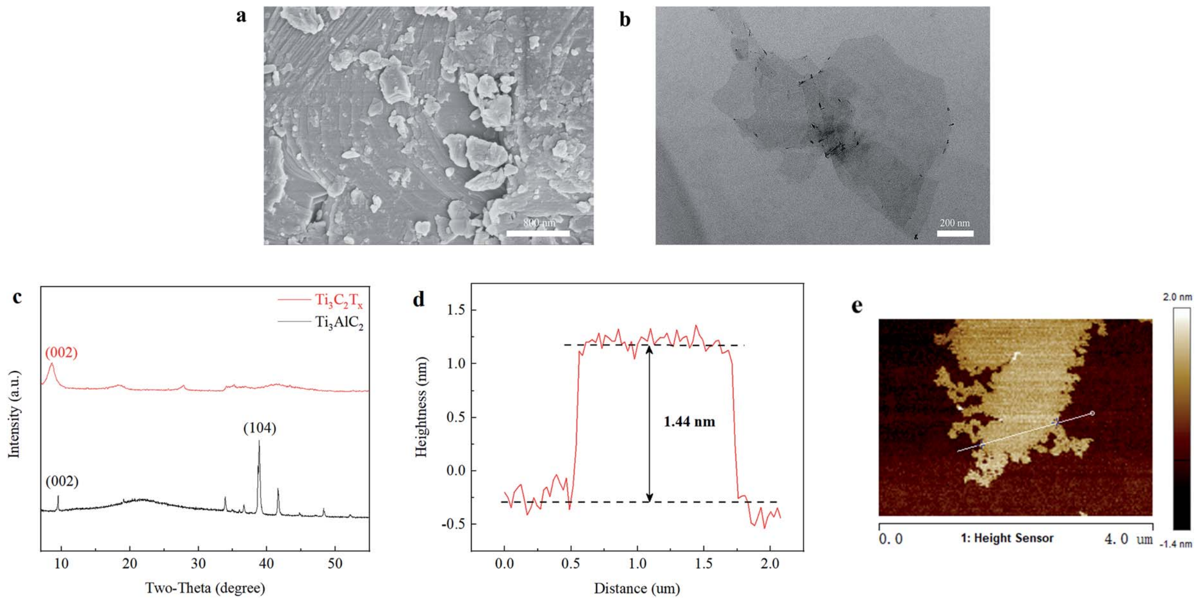

Fig. 1 Scanning electron microscopy (SEM) (a) of Ti_3AlC_2; transmission electron microscopy (TEM) (b), X-ray diffraction (XRD) (c), and atomic force microscopy (AFM) (d and e) of $Ti_3C_2T_x$.

where R_A and R_B represent the retention of solute A and solute B, respectively.

3. Results and discussion

3.1 Microstructure of $Ti_3C_2T_x$

Fig. 1(a) shows an SEM image of the Ti_3AlC_2 powder with a prominent lamellar structure. A few loose flakes were perceived on the surface, thereby indicating its suitability for exfoliation as a $Ti_3C_2T_x$ precursor. The previously reported mild method was used for *in situ* etching of Ti_3AlC_2.[33] The raw material and the product were examined by XRD to identify the crystallization properties and d-spacing of the product, and the resulting XRD patterns are shown in Fig. 1(c). The diffraction peak (002) at a slight angle corresponded to the characteristic diffraction peak of $Ti_3C_2T_x$, and the unique peak (104) of Ti_3AlC_2 almost disappeared completely, which proved that the preparation of $Ti_3C_2T_x$ was successful.[34] Compared with the diffraction peak of the raw material, the (002) diffraction peak of $Ti_3C_2T_x$ was displaced by a slight angle due to atomic intercalation, thereby indicating larger layer spacing.

After ultrasound-assisted exfoliation, the precursor Ti_3AlC_2 was delaminated to form several layers of MXene nanosheets. The TEM image of $Ti_3C_2T_x$ nanosheets is shown in Fig. 1(b). The TEM image shows that 3–4 layers of nanosheets are stacked together, thereby presenting a 2D thin layer structure with a lateral dimension of approximately 700–800 nm.

To determine whether the $Ti_3C_2T_x$ nanosheet had a single layer or a few layers, AFM was used to characterize the thickness of the nanosheet. Fig. 1(d and e) shows the AFM image of $Ti_3C_2T_x$. The theoretical thickness of the monolayer $Ti_3C_2T_x$ nanosheets was 1.51 nm.[35] According to the AFM image, the height difference between the nanosheets was 1.44 nm, which was roughly consistent with that in a previous report.[36] Monolayer $Ti_3C_2T_x$ nanosheets were successfully prepared.

Scheme 1 shows a schematic representation of the $Ti_3C_2T_x$/NF membrane synthesis. The PA separation layer, $Ti_3C_2T_x$, and PIP were bonded by van der Waals forces and hydrogen bonding to form thin-film nanocomposite membranes, and their separation characteristics were explored.

3.2 Microstructure of $Ti_3C_2T_x$/NF membranes

SEM was used to examine the surface morphology of the NF membrane, and the results are presented in Fig. 2. Due to the rapid polycondensation reaction between the aqueous monomer PIP and the organic monomer TMC, the membrane surface showed a typical smooth nodular structure, which was consistent with previous reports.[37,38] This phenomenon might have been due to the pre-storage of aqueous monomer in the membrane pores, which caused a difference in the adsorption depth and adsorption amount of monomer inside and outside the pores, thereby leading to a variable monomer diffusion rate in the IP process.[39–44] In addition, bulges around the nodular structure were observed, resembling a bubble-like structure, which might have been due to the doping of MXene nanosheets. The highly enhanced PIP adsorption by the MXene nanosheets facilitates the reaction rate of the IP process.[39] Then, the fresh PA layer was jacked up from the membrane pores, the solution inside the pore spilled out from its edges, forming bubble-like bulges. In addition, the hydrophilic groups on the surface of MXene nanosheets attract water molecules and promote their retention during the IP process. Moreover, the thin flake structure representing MXene nanosheets appeared on the M2 surface under high magnification (Fig. S1†). EDS analysis of the membrane surface also confirmed the successful doping of $Ti_3C_2T_x$ on the membrane surface (Fig. S2†). With the above results, it can be concluded that the MXene nanosheets were successfully embedded into the PA layer.[30] The regulation of the PA layer was conducted by the MXene-assisted IP process, which enhanced the adsorption of the PIP and attracted water molecules, and these changes were expected to improve the performance of the resultant NF membranes.

AFM scanning was used to examine the influence of MXene doping on surface roughness. The AFM images and surface characteristics of the original and produced membranes are shown in Fig. 3 and Table 1. Compared with the naked PA-NF membrane, the surface of the thin-film nanocomposite membrane was coarser when the doping content of $Ti_3C_2T_x$ increased to 0.002 wt%. The PA layer's remarkable sensitivity to the presence of nanomaterials could explain the variance in its surface morphology. The inducement of MXene creates

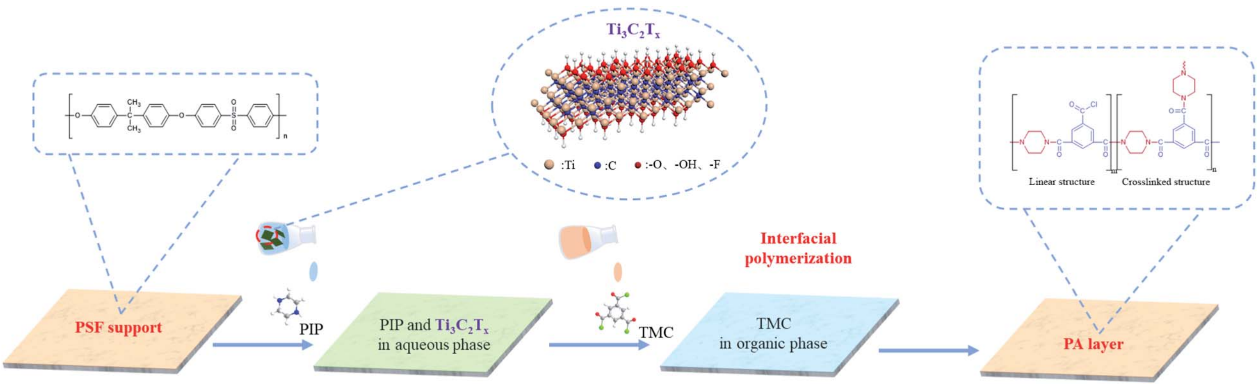

Scheme 1 Synthesis process of $Ti_3C_2T_x$/nanofiltration (NF) membranes.

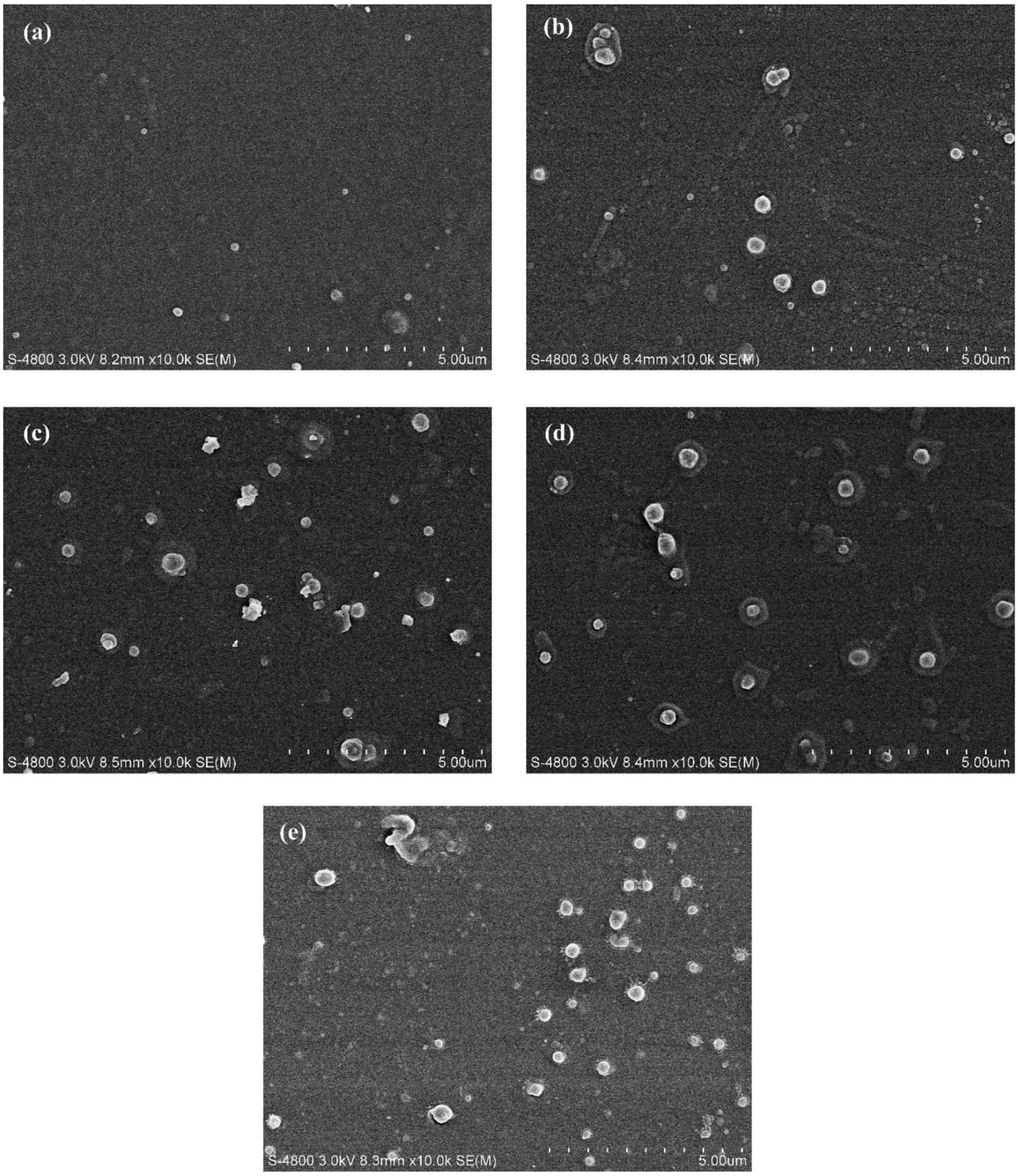

Fig. 2 Scanning electron microscopy (SEM) surface morphologies of M0, M1, M2, M3, and M4 (a–e).

a bubble-like structure of bumps on the PA layer, thereby increasing the surface roughness of the TFN membrane. The higher surface roughness could contribute to greater increased water contact area, which would be beneficial for the improvement of water permeability. When the mass percentage of $Ti_3C_2T_x$ increased to 0.005 wt%, the membrane surface became smooth owing to the increased hydrophilicity caused by $Ti_3C_2T_x$ and the effect on the diffusion rate. Due to the diffusion of the aqueous monomer into the organic phase is the rate-limiting step in the IP reaction.[45] Higher nanomaterial loading might have hindered the diffusion of aqueous phase monomers, resulting in a smoother membrane surface, consistent with previous studies.[46]

The surface functional groups on the membranes were detected by FTIR, as illustrated in Fig. 4(a). FTIR has a penetration depth of a few hundred nanometers to a few microns, making it helpful for detecting PA top layers and PSF support layers.[47] Weak aromatic amide peaks were seen in all membranes at 1629 cm^{-1}, which is the C=O stretching vibration of amide I, originates from poly (piperazine amide). When $Ti_3C_2T_x$ was added, the 3406 cm^{-1} O–H stretching vibration increased, which may be accounted for the hydroxyl (–OH) functional groups on the $Ti_3C_2T_x$ surface. Additionally, the peak strength of 1489 cm^{-1} for O–H bending from carboxyl and 1508 cm^{-1} for N–H in-plane bending reduced, owing to the influence of nanomaterial doping. It might be explained for $Ti_3C_2T_x$ addition helps storage aqueous monomer in IP process, accelerating the IP reaction rare, leading to unreacted TMC hydrolysis to –COOH decreased the associated peak. Moreover, the hydroxyl of MXene nanosheets forms hydrogen bonds with

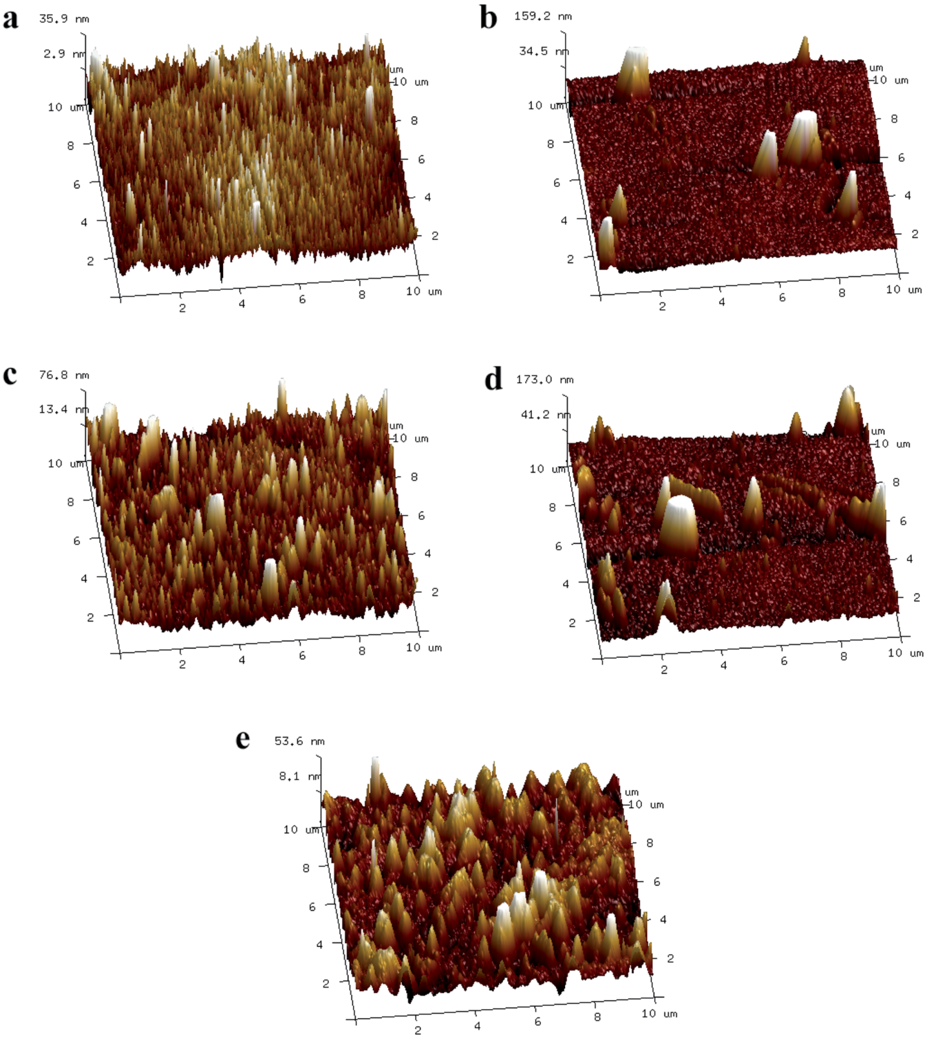

Fig. 3 Atomic force microscopy (AFM) 3D surface morphologies of M0, M1, M2, M3, and M4 (a–e).

Table 1 Surface properties of the thin-film composite (TFC) membranes prepared at different $Ti_3C_2T_x$ loading rates

$Ti_3C_2T_x$ content (wt%)	R_a	R_q
0	6.72	8.95
0.001	10.2	23.7
0.002	11.8	16.3
0.005	15.6	29.1
0.010	10.4	13.8

the piperazine group, limiting the N–H stretching vibration and thus decreasing the peak intensity at 1508 cm^{-1}.

Benefiting from the high detection accuracy of XPS, to verify whether $Ti_3C_2T_x$ nanosheets were successfully doped into the PA cortex, a series of thin-film NF membranes were prepared according to the concentration in Table 1, and XPS analysis was performed on the M0 and M2 membranes. The wide-scan XPS spectra of M0 and M2 are shown in Fig. 4(b). In the M2 spectrum, there were almost no peaks corresponding to Ti and F, which might be due to the ultra-low load of MXene nanosheets and the bulk of MXene being covered by PA. The results of the XPS content analysis for the M0 and M2 membranes are shown in Table 2. The surface of the M0 membrane contained no Ti and F elements, whereas the atomic mass fractions of Ti and F on the surface of the M2 membrane were 0.20% and 0.29%, respectively, thereby confirming the successful doping of MXene. Compared with the original membrane, the element composition of the modified membrane was slightly different. The modified membrane had a lower O/N ratio, corresponding to a higher degree of cross-linking.[39,47] It was thought that the hydrogen bonds between piperazine monomers and MXene nanosheet could control the release of piperazine and then affect the IP process, promoting the formation of a tight PA barrier layer.

To investigate the improvement of hydrophilic properties of MXene doping on the membrane surface, the water contact angle of the M0 and M2 membranes was measured, and the results are shown in Fig. 5(a–e). The hydrophilicity of the membrane surface increased as the water contact angle

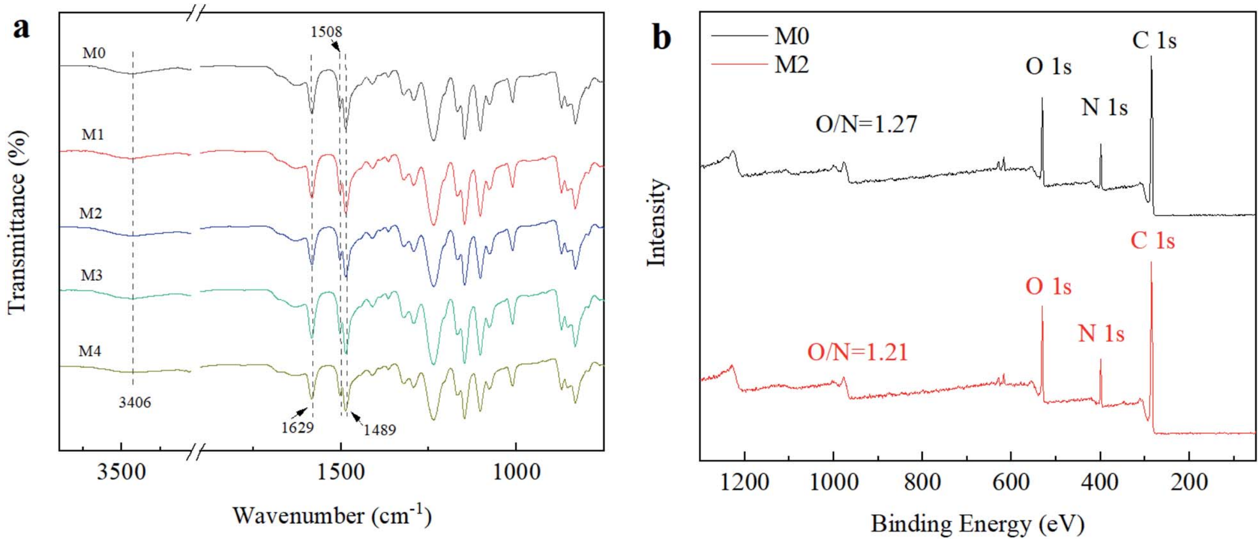

Fig. 4 Fourier transform infrared spectroscopy (FTIR) spectra of M0, M1, M2, M3, and M4 (a) and X-ray photoelectron spectroscopy (XPS) spectra of M0 and M2 (b).

decreased when the surface shape of the membranes was similar.[48] The water contact angle of the membrane reduced as the $Ti_3C_2T_x$ nanosheet doping increased, indicating that $Ti_3C_2T_x$ doping in the PA layer could effectively improve the membrane's hydrophilicity.[49,50] The improvement in hydrophilicity is related to the hydrophilic functional groups (–OH and –O) on the surface of $Ti_3C_2T_x$. The powerful hydrophilic groups can attract water molecules and form a thin hydration layer on the membrane surface *via* hydrogen bond. In addition, the oxygen functional groups have a strong water affinity. This, in turn, demonstrates that $Ti_3C_2T_x$ was successfully embedded in the PA layer. It is implied that the hydrophilic MXene-assisted NF membranes would exhibit outstanding permeability and anti-fouling performance.[51]

The charge characteristics of the membrane surface were evaluated using the zeta potential, as shown in Fig. 6(a). The isoelectric point of the original membrane without $Ti_3C_2T_x$ doping and the TFN membrane doped with a $Ti_3C_2T_x$ mass fraction of 0.002 wt% was 3.2. At pH > 6, the surfaces of both the initial and modified membranes doped with $Ti_3C_2T_x$ were negatively charged.[50] The zeta potential of the M2 membrane decreased and became more negative compared with that of the original membrane. Owing to the abundance of negative groups such as –OH and –F in the doped $Ti_3C_2T_x$, the electronegativity of the membrane surface was improved. MXene-mediated PA layer would strengthen the anionic dye repulsion by electrostatic interaction, therefore enhancing both the selectivity and fouling resistance of the modified membrane.

The membranes' MWCO was determined using PEG of different molecular weights. Fig. 6(b) shows the PEG retention rates of the M0 and M2 membranes. The MWCO of the pristine membrane is 371, whereas the MWCO of the M2 membrane modified by MXene is 360. The high degree of cross-linking corresponds to narrower pore sizes, which is consistent with the chemical characteristics shown by XPS. It is further demonstrated that the doping of MXene helps form a dense and defect-free PA layer, reducing the formation of non-selective pores, which would positively affect the separation efficiency.

3.3 Separation performance of $Ti_3C_2T_x$/NF membranes

The separation effectiveness of the $Ti_3C_2T_x$/NF membrane was tested under 0.35 MPa pressure with various feed solutions in this study. The water flux of the initial and modified NF membranes is shown in Fig. 7(a). The flux of all the membranes modified with $Ti_3C_2T_x$ nanosheets significantly improved. The original PA membrane had a pure water flux of 28.55 L m^{-2} h^{-1}. When $Ti_3C_2T_x$ nanosheets were introduced into the functional PA layer with low loading (0.002 wt%), the pure water flux attained 45.12 L m^{-2} h^{-1}. Compared with the membrane without $Ti_3C_2T_x$ doping, the water flux increased by 58%. The pure water flux decreased slightly as the $Ti_3C_2T_x$ loading was

Table 2 X-ray photoelectron spectroscopy (XPS) analysis of the element content on M0 and M2 membrane

	C 1s (%)	O 1s (%)	N 1s (%)	Ti 2p (%)	F 1s (%)	O/N ratio	*D* (%)
M0	72.96	15.11	11.93	0	0	1.27	64.72
M2	72.57	14.77	12.20	0.19	0.28	1.21	71.41

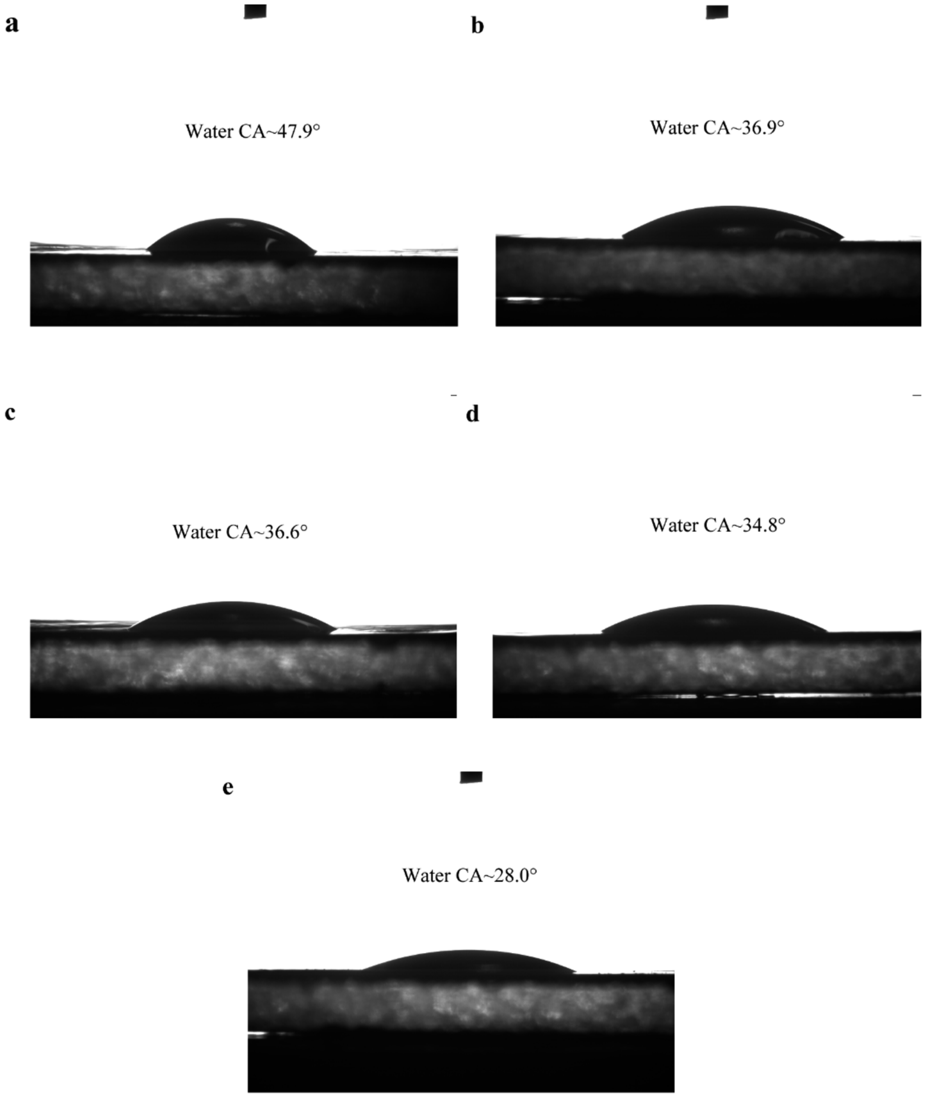

Fig. 5 Water contact angle of M0, M1, M2, M3, and M4 (a–e).

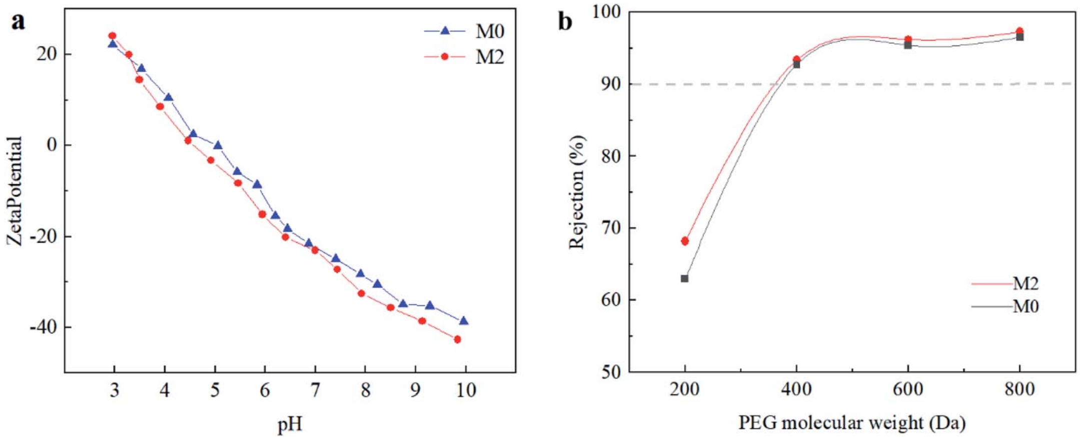

Fig. 6 Zeta potential (a) and MWCO (b) of M0 and M2.

raised further, though it is still more significant than the pristine membrane without modification.

The increase in water permeability may be closely related to the doping of $Ti_3C_2T_x$ nanosheets and the resulting change in the surface morphology of the PA layer. For one thing, the introduction of $Ti_3C_2T_x$ nanosheets leads to bubble-like bulges on the surface of the PA layer, increasing the effective water contact area. For another, the introduction of $Ti_3C_2T_x$ nanosheets disrupted the polymer chain packing, increasing the system's free volume.[22] Meanwhile, the hydrophilic functional groups such as OF and –OH introduced during the preparation of $Ti_3C_2T_x$ nanosheets can attract water molecules in the membrane matrix and facilitate their passage through the membrane.[31,50] In addition, the layered structure of $Ti_3C_2T_x$ may provide additional nanoscale channels for the rapid passage of water molecules through the membrane.[52,53] When the introduction of $Ti_3C_2T_x$ is in a high state (>0.005 wt%), the higher nanomaterial loading results in a smoother membrane surface, reducing the effective water contact area, thereby resulting in a decrease in permeability.[4,54]

The influence of the introduction of $Ti_3C_2T_x$ nanosheets on the efficiency of TFN membranes in retaining salt ions was further investigated, with the results shown in Fig. 7 (b). The retention of salt ions by all membranes was ranked as Na_2SO_4 > $MgSO_4$ > NaCl, which could be attributed to the difference in the selectivity of the charged NF membranes for different ions. It is generally considered a result of the combined size sieving effect and the Donnan effect. The $Ti_3C_2T_x$/NF membranes were electronegative at pH > 6. Owing to the Donnan effect, the $Ti_3C_2T_x$/NF membrane repels high-valence ions ($SO4^{2-}$) more strongly than low-valence ions (Cl^-), which is manifested by the high retention rate of SO_4^{2-}.[55] The electrostatic gravitational force of Mg^{2+} is stronger than that of Na^+; the Donnan effect is weakened to a certain extent; thus, the retention rate of the $Ti_3C_2T_x$/NF membrane for Na_2SO_4 was slightly higher than that for $MgSO_4$. Significantly, the rejection of both salt ions improved under a lower $Ti_3C_2T_x$ loading. First of all, it could be attributed to the abundant –OH groups and –F above the $Ti_3C_2T_x$ nanosheet.[23] The negatively charged groups made the zeta potential on the membrane surface more negative, thereby amplifying the electrostatic repulsion between the solute and the membrane surface. The enhanced Donnan exclusion effect led to higher repulsion rates.[56] Besides, the low concentration of MXene doping enhances the cross-linking degree of PA layers; the smaller pore size increases the repulsion of the membranes to salt ions through the size exclusion effect. In the end, the layered structure of MXene, allowing better distribution and diffusion of monomers during the IP reaction and reduces the formation of non-selective pores.[57] In contrast, the salt rejection rate decreased when a higher $Ti_3C_2T_x$ load was reached. When excessive $Ti_3C_2T_x$ was added, it reduced the cross-linking degree of the PA layer, which could cause looseness of the structure and influence the integrity of the active layer.[30] The size exclusion effect of the PA layer was eventually weakened by the negative effects mentioned above, therefore reducing the salt rejection rate. The M2 membrane showed great performance for both water permeation and salt rejection, and due to this reason, which was chosen to explore the dye separation performance further.

Four kinds of organic dyes with different types of charges were chosen to evaluate the dye removal ability of the $Ti_3C_2T_x$/NF membrane, as shown in Fig. 8(a). The M2 membrane showed high retention (>97.5%) for all four dyes. Meanwhile, the flux of the M2 membrane with the four dye solutions with different charge types was similar (CR: 41.83 L m^{-2} h^{-1}, MO: 43.52 L m^{-2} h^{-1}, CV: 42.77 L m^{-2} h^{-1}, and MB: 45.10 L m^{-2} h^{-1}). The two dyes with higher molecular weights (CR and CV) exhibited a higher rejection rate (>99.4%), which might have been attributed to the size exclusion effect.[58] Although the molecular weights of MO and MB were similar, there were some variations in rejection. This phenomenon can be explained by the electrostatic repulsion effect.[59] The retention of the anionic dye MO (98.71%) was higher than that of the cationic dye MB (97.27%) due to the enhanced electrostatic repulsion by the higher negative zeta potential on the

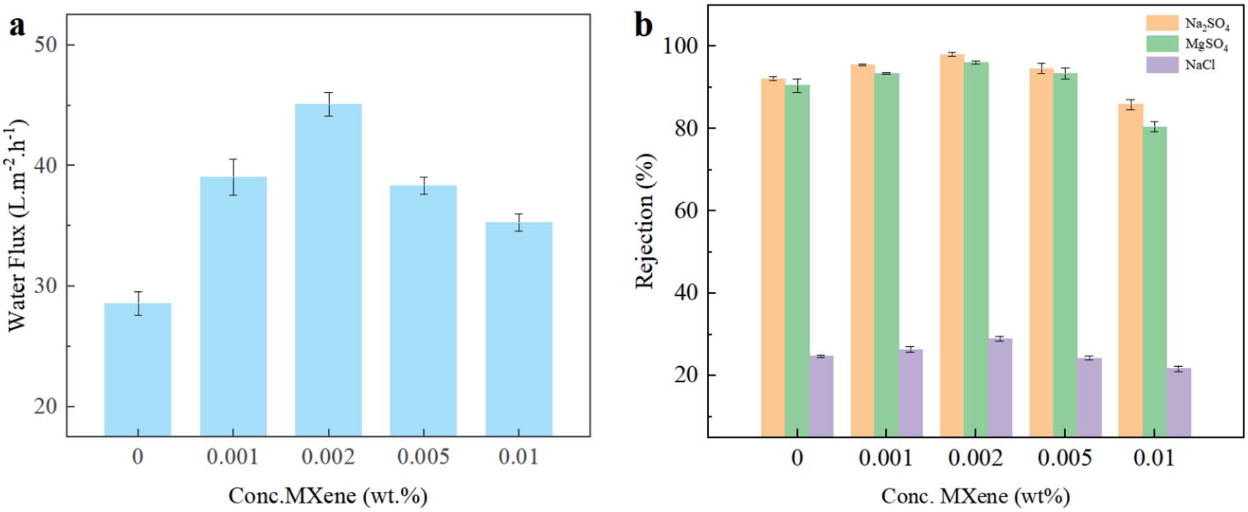

Fig. 7 Pure water flux (a); Na_2SO_4, $MgSO_4$ and NaCl rejection of M0, M1, M2, M3, and M4 (b).

membrane surface, owing to the introduction of MXene nanosheets. Additionally, the effective pore size of M2 shows a slight shrinking of 5.8% to 0.52 nm, which is smaller than the hydrated ionic radius of most multivalent ions and tested dyes, thereby promoting the sieving performance. The molecular structure of the dye is shown in Fig. S3.†

Effective separation of dye molecules and inorganic salts is the key to the purification process of crude dyes.[59–62] Owing to the high NaCl permeability and dye retention performance of the $Ti_3C_2T_x$/NF membranes, the prepared membrane should have excellent selectivity for NaCl and various dye molecules. Fig. 8(b and c) shows the $Ti_3C_2T_x$/NF membrane's selective separation effect for the dye/salt mixture solution. The feed solution consisted of 2000 ppm NaCl and 100 ppm dye (CR and CV). For the two dye molecules with different charges, the M2 membrane showed nearly 100% rejection while maintaining a high permeability for NaCl. The separation factors of NaCl/CR and NaCl/CV were computed using eqn (4) and were calculated as 820.0 and 500.5, respectively. In addition, the water flux and dye/NaCl separation performance of the $Ti_3C_2T_x$/NF membrane were compared with those of other reported membranes.[22,59–65] The $Ti_3C_2T_x$/NF membrane exhibited superior permeability and dye/NaCl separation performance compared with those of other NF membranes, making it an attractive candidate for dye/salt separation membrane in the future.

3.4 Antifouling performance of $Ti_3C_2T_x$/NF membranes

An anti-fouling experiment with $Ti_3C_2T_x$/NF membranes was conducted using a 0.1 g L^{-1} CR aqueous solution as feed. Each dynamic fouling experiment consisted of a 60 min baseline stage, 60 min fouling stage, and 60 min recovery stage after cleaning. The normalized water flux distribution of the M2 membrane during the fouling process is shown in Fig. 9(a). The water flux of the tested membranes decreased significantly after exposure to the dye solution, which was caused by concentration polarization and membrane contamination. After backwashing, the flux recovered to 85.75% and showed slight fluctuation, indicating excellent anti-fouling performance. It could be speculated that the doping of $Ti_3C_2T_x$ could attract water molecules, thereby forming a tight water hydration layer on the membrane surface.[30] Thus weakened the interaction between the dye and the membrane surface significantly and reduced the adsorption capacity of the dye. Additionally, the negatively charged groups on MXene-mediated PA layer reduce the zeta potential of the membrane surface, thereby enhancing the electrostatic repulsion effect, contributing to the rejection of anionic dyes by the PA layer. Therefore, the MXene-mediated NF membrane exhibited superior anti-fouling ability, making it dominant in the practical dye/salt separation process.

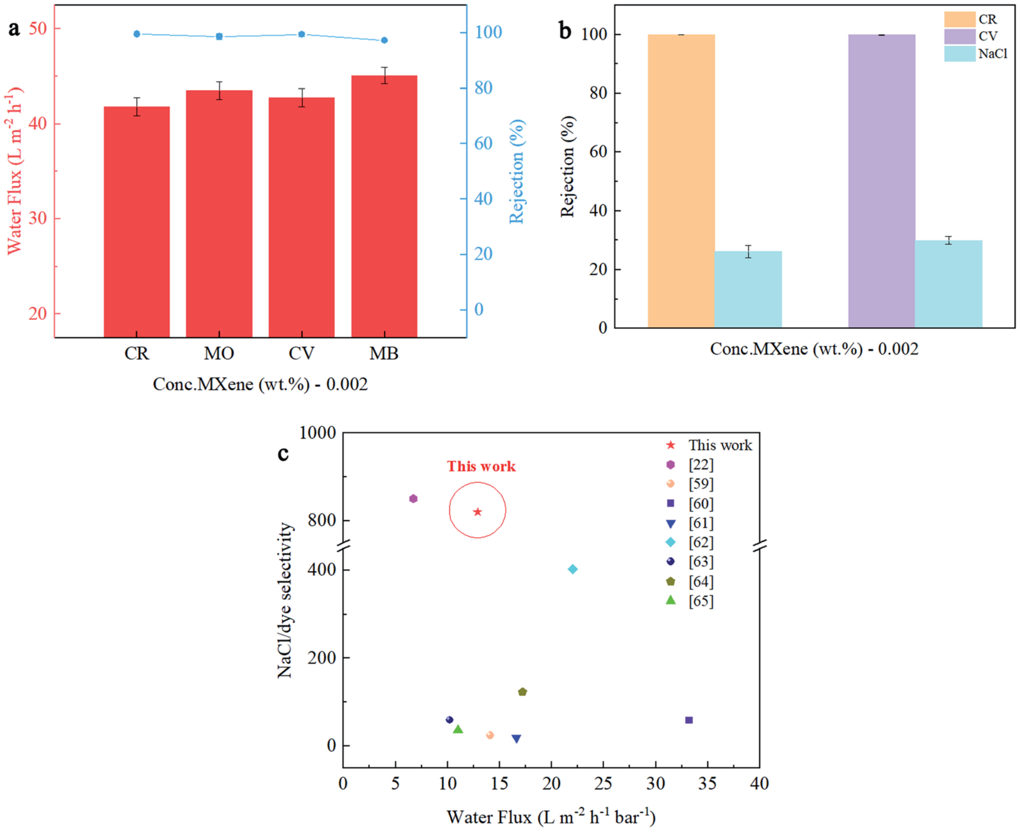

Fig. 8 Nanofiltration (NF) performance of M2 with diverse dye solutions (a); rejection performance of M2 with Congo Red (CR)/NaCl and Crystal Violet (CV)/NaCl solutions (b); comparison of NaCl/dye selectivity *versus* water flux in this study and other studies (c).

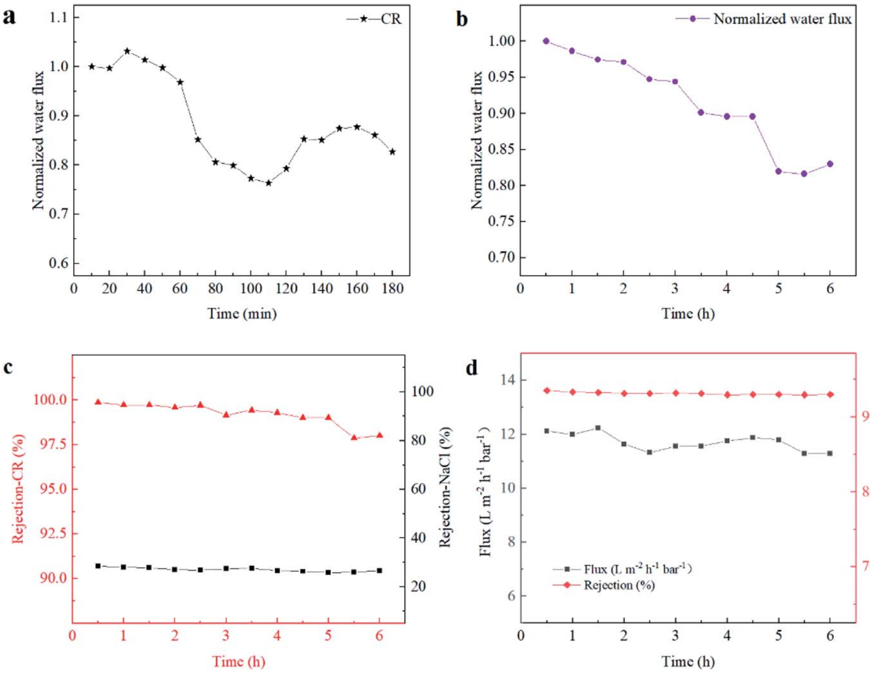

Fig. 9 Antifouling test (a) and long-term filtration (b–d) of M2 (normalized water flux (b); CR rejection (c); Na_2SO_4 rejection (d)).

3.5 Long-term stability of $Ti_3C_2T_x$/NF membranes

To evaluate the $Ti_3C_2T_x$/NF membrane's long-term stability, a filtration testing was conducted at 0.35 MPa for 6 h. The mixed solution consisted of 2000 ppm NaCl and 100 ppm dye (CR), the results are shown in Fig. 9(b and c). During the continuous filtration process, the membranes maintained high dye retention (approximately 99.20%) and low NaCl retention (approximately 27.0%), and the maximum flux decline was reduced to 18.0% after 300 min. These results indicated that the $Ti_3C_2T_x$/NF membrane had high NaCl/dye selectivity and good long-term stability. It could be attributed to the hydrogen bond interaction of MXene with PSF-based membrane and the PA layer, forming a higher crosslinking PA layer, thereby enhancing the membrane's mechanical properties. The M2 membrane also exhibited excellent performance stability in a 6 h test with 2000 ppm Na_2SO_4 solution (Fig. 9(d)). In addition, the PA layer was intact on the surface PSF substrate with outstanding integrity and mechanical strength (Fig.S4 and S5†). As a result, the $Ti_3C_2T_x$/NF membrane with the optimized $Ti_3C_2T_x$ doping amount was able to overcome the balance between water permeability and salt selectivity and therefore has a great capability for dye and salt separation.

4. Conclusion

A novel PA-NF membrane with an enhanced nanostructure was prepared *via in situ* IP with the incorporation of MXene nanosheets. This MXene-regulation polyamide membrane exhibited enhancing water permeability from 28.55 L m^{-1} h^{-1} to 45.12 L m^{-1} h^{-1}, whereas the salt retention rate remained essentially unchanged. Besides, the retention rate of the anionic dyes (CR and CV) was 99.4%. The dye/monovalent salt separation coefficient reached 820, thereby demonstrating excellent dye concentration performance. The increase in performance could be attributed to the MXene-assisted IP strategy, which reduced the formation of non-selective pores. At the same time, the bubble-like nodule was appeared on the membrane surface, which endowed the PA layer with an increased effective permeable area. In addition, an effective dye anti-fouling PA layer was successfully constructed *via* MXene-mediated IP process, which was imperative to fouling resistance. Hence, the study highlights the great potential of the MXene-regulated nanostructure of the PA layer in the manufacturing of high-performance dye/salt separation membranes.

Conflicts of interest

There are no conflicts to declare.

Acknowledgements

The work was financially supported by the National Natural Science Foundation of China (No. 51978239).

References

1 Q. Li, Z. Liao, X. Fang, J. Xie, L. Ni, D. Wang, J. Qi, X. Sun, L. Wang and J. Li, *Desalination*, 2020, **479**, 114343.
2 Y. He, G.-M. Li, H. Wang, Z.-W. Jiang, J.-F. Zhao, H.-X. Su and Q.-Y. Huang, *J. Taiwan Inst. Chem. Eng.*, 2009, **40**, 289–295.
3 S. Yu, C. Gao, H. Su and M. Liu, *Desalination*, 2001, 97–100.
4 C. Zhang, K. Wei, W. Zhang, Y. Bai, Y. Sun and J. Gu, *ACS Appl. Mater. Interfaces*, 2017, **9**, 11082–11094.

5 P. Jin, S. Chergaoui, J. Zheng, A. Volodine, X. Zhang, Z. Liu, P. Luis and B. Van der Bruggen, *J. Hazard. Mater.*, 2021, **421**, 126716.

6 J. Luo and Y. Wan, *J. Membr. Sci.*, 2013, **438**, 18–28.

7 Y. Mansourpanah, A. Ghanbari, H. Yazdani, A. G. Mohammadi and A. Rahimpour, *Desalination*, 2021, **511**, 115109.

8 Q. Zhao, D. L. Zhao and T.-S. Chung, *J. Membr. Sci.*, 2021, **625**, 119158.

9 Y. Song, X. Bai, N. Zhang, Z. Lu, M. Zhu, Y. Wang and K. Jiang, *J. Membr. Sci.*, 2021, **636**, 119580.

10 A. M. Saira Bano, S.-J. Kim and K.-H. Lee, *J. Mater. Chem. A*, 2015, **3**, 2065–2071.

11 Y.-F. Mi, G. Xu, Y.-S. Guo, B. Wu and Q.-F. An, *J. Membr. Sci.*, 2020, **601**, 117795.

12 A. Anand, B. Unnikrishnan, J.-Y. Mao, H.-J. Lin and C.-C. Huang, *Desalination*, 2018, **429**, 119–133.

13 M. Jahanshahi, A. Rahimpour and M. Peyravi, *Desalination*, 2010, **257**, 129–136.

14 B. Tian, P. Hu, S. Zhao, M. Wang, Y. Hou, Q. J. Niu and P. Li, *Desalination*, 2021, **512**, 115118.

15 J. R. Werber, A. Deshmukh and M. Elimelech, *Environ. Sci. Technol. Lett.*, 2016, **3**, 112–120.

16 J. Yin, G. Zhu and B. Deng, *Desalination*, 2016, **379**, 93–101.

17 S. Yang, Q. Jiang and K. Zhang, *J. Membr. Sci.*, 2020, **604**, 118052.

18 S. Seyyed Shahabi, N. Azizi and V. Vatanpour, *Sep. Purif. Technol.*, 2019, **215**, 430–440.

19 S. Abdikheibari, W. Lei, L. F. Dumée, A. J. Barlow and K. Baskaran, *Appl. Surf. Sci.*, 2019, **488**, 565–577.

20 J. Z. Zhipeng Liao, X. Li and B. Van der Bruggen, *Sep. Purif. Technol.*, 2021, **266**, 118567.

21 X. Chen, W. Wang, L. Zhu, C. Liu, F. Cui, N. Li and B. Zhang, *ACS Appl. Nano Mater.*, 2020, **4**, 673–682.

22 C.-C. Ye, F.-Y. Zhao, J.-K. Wu, X.-D. Weng, P.-Y. Zheng, Y.-F. Mi, Q.-F. An and C.-J. Gao, *Chem. Eng. J.*, 2017, **307**, 526–536.

23 G. R. Berdiyorov and K. A. Mahmoud, *Appl. Surf. Sci.*, 2017, **416**, 725–730.

24 X. Tong, S. Liu, D. Qu, H. Gao, L. Yan, Y. Chen and J. Crittenden, *J. Membr. Sci.*, 2021, **622**, 119042.

25 K. Meidani, Z. Cao and A. Barati Farimani, *ACS Appl. Nano Mater.*, 2021, **4**, 6145–6151.

26 Y. Li, R. Dai, H. Zhou, X. Li and Z. Wang, *ACS Appl. Nano Mater.*, 2021, **4**, 6328–6336.

27 M. Rezakazemi, A. Arabi Shamsabadi, H. Lin, P. Luis, S. Ramakrishna and T. M. Aminabhavi, *Renew. Sustain. Energy Rev.*, 2021, **143**, 110878.

28 K. Z. Kaili Gong, X. Qian, C. Shi and B. Yu, *Composites, Part B*, 2021, **217**, 108867.

29 L. L. Jian Li, Y. Xu, J. Zhu, F. Liu, J. Shen, Z. Wang and J. Lin, *Chem. Eng. J.*, 2022, **427**, 132070.

30 X. Wang, Q. Li, J. Zhang, H. Huang, S. Wu and Y. Yang, *J. Membr. Sci.*, 2020, **603**, 118036.

31 Q. Xue and K. Zhang, *J. Membr. Sci.*, 2021, **640**, 119808.

32 C. P. Koutsou and A. J. Karabelas, *J. Membr. Sci.*, 2012, **399–400**, 60–72.

33 M. Alhabeb, K. Maleski, B. Anasori, P. Lelyukh, L. Clark, S. Sin and Y. Gogotsi, *Chem. Mater.*, 2017, **29**, 7633–7644.

34 M. Naguib, M. Kurtoglu, V. Presser, J. Lu, J. Niu, M. Heon, L. Hultman, Y. Gogotsi and M. W. Barsoum, *Adv. Mater.*, 2011, **23**, 4248–4253.

35 Y. Ying, Y. Liu, X. Wang, Y. Mao, W. Cao, P. Hu and X. Peng, *ACS Appl. Mater. Interfaces*, 2015, **7**, 1795–1803.

36 L. Ding, Y. Wei, Y. Wang, H. Chen, J. Caro and H. Wang, *Angew. Chem., Int. Ed. Engl.*, 2017, **56**, 1825–1829.

37 A. K. Ghosh and E. M. V. Hoek, *J. Membr. Sci.*, 2009, **336**, 140–148.

38 Z. Tan, S. Chen, X. Peng, L. Zhang and C. Gao, *Science*, 2018, **360**, 518–521.

39 F. Zhang, J. B. Fan and S. Wang, *Angew. Chem., Int. Ed. Engl.*, 2020, **59**, 21840–21856.

40 L. E. Peng, Z. Yao, X. Liu, B. Deng, H. Guo and C. Y. Tang, *Environ. Sci. Technol.*, 2019, **53**, 9764–9770.

41 X. Song, B. Gan, S. Qi, H. Guo, C. Y. Tang, Y. Zhou and C. Gao, *Environ. Sci. Technol.*, 2020, **54**, 3559–3569.

42 X.-H. Ma, Z.-K. Yao, Z. Yang, H. Guo, Z.-L. Xu, C. Y. Tang and M. Elimelech, *Environ. Sci. Technol. Lett.*, 2018, **5**, 123–130.

43 Q. Zhang, Z. Zhang, L. Dai, H. Wang, S. Li and S. Zhang, *J. Membr. Sci.*, 2017, **537**, 372–383.

44 X. Zhu, X. Zhang, J. Li, X. Luo, D. Xu, D. Wu, W. Wang, X. Cheng, G. Li and H. Liang, *J. Membr. Sci.*, 2021, **635**, 119536.

45 V. Freger, *Langmuir*, 2005, **21**, 1884–1894.

46 W. Zhao, H. Liu, N. Meng, M. Jian, H. Wang and X. Zhang, *J. Membr. Sci.*, 2018, **565**, 380–389.

47 Y.-N. K. Chuyang, Y. Tang and J. O. Leckie, *Desalination*, 2009, **242**, 149–167.

48 Y.-N. K. Chuyang, Y. Tang and J. O. Leckie, *Desalination*, 2009, **242**, 168–182.

49 M. Ghidiu, M. R. Lukatskaya, M. Q. Zhao, Y. Gogotsi and M. W. Barsoum, *Nature*, 2014, **516**, 78–81.

50 Z. Ling, C. E. Ren, M. Q. Zhao, J. Yang, J. M. Giammarco, J. Qiu, M. W. Barsoum and Y. Gogotsi, *Proc. Natl. Acad. Sci. U. S. A.*, 2014, **111**, 16676–16681.

51 Y. Cheng, Y. Pu and D. Zhao, *Chem. Asian J.*, 2020, **15**, 2241–2270.

52 I. Ihsanullah, *Chem. Eng. J.*, 2020, **388**, 124340.

53 X. Xie, C. Chen, N. Zhang, Z.-R. Tang, J. Jiang and Y.-J. Xu, *Nat. Sustain.*, 2019, **2**, 856–862.

54 H. Zhang, L. Bin, J. Pan, Y. Qi, J. Shen, C. Gao and B. Van der Bruggen, *J. Membr. Sci.*, 2017, **539**, 128–137.

55 D. Vezzani and S. Bandini, *Desalination*, 2002, **149**, 477–483.

56 W. Yang, H. Xu, W. Chen, Z. Shen, M. Ding, T. Lin, H. Tao, Q. Kong, G. Yang and Z. Xie, *Desalination*, 2020, **479**, 114330.

57 G. M. Geise, H. B. Park, A. C. Sagle, B. D. Freeman and J. E. McGrath, *J. Membr. Sci.*, 2011, **369**, 130–138.

58 H. E. Karahan, K. Goh, C. J. Zhang, E. Yang, C. Yildirim, C. Y. Chuah, M. G. Ahunbay, J. Lee, S. B. Tantekin-Ersolmaz, Y. Chen and T. H. Bae, *Adv. Mater.*, 2020, **32**, 1906697.

59 X.-l. Wang, W. Qin, L.-x. Wang, K.-y. Zhao, H.-c. Wang, H.-y. Liu and J.-f. Wei, *Sep. Purif. Technol.*, 2020, **253**, 117475.

60 S. Liu, Z. Wang and P. Song, *ACS Sustainable Chem. Eng.*, 2018, **6**, 4253–4263.

61 Y. F. Mi, N. Wang, Q. Qi, B. Yu, X. D. Peng and Z. H. Cao, *Sep. Purif. Technol.*, 2020, **248**, 117079.

62 T. Zhang, P. Li, S. Ding and X. Wang, *Sep. Purif. Technol.*, 2021, **270**, 118802.

63 W. Ye, J. Lin, R. Borrego, D. Chen, A. Sotto, P. Luis, M. Liu, S. Zhao, C. Y. Tang and B. Van der Bruggen, *Sep. Purif. Technol.*, 2018, **197**, 27–35.

64 G. Gong, P. Wang, Z. Zhou and Y. Hu, *ACS Appl. Mater. Interfaces*, 2019, **11**, 7349–7356.

65 L. Wang, S. Ji, N. Wang, R. Zhang, G. Zhang and J.-R. Li, *J. Membr. Sci.*, 2014, **452**, 143–151.